

space vector \vec{I}_{res} consists of the fundamental wave current \vec{I}_1 and the high-frequency current \vec{I}_{hf} as the consequence of the test signal.

$$\vec{I}_{res} = \vec{I}_1 + \vec{I}_{hf} \quad (4)$$

$$= (I_{1\alpha} + j \cdot I_{1\beta}) + (I_{hf\alpha} + j \cdot I_{hf\beta}) \quad (5)$$

For calculation of the complex impedance and decoupling of the test signal from the field-oriented control, these two currents have to be separated.

The extraction of the high-frequency current can be made by a Fast Fourier Transformation (FFT) of \vec{I}_{res} . The FFT demands a high computational effort and delivers the amplitude and the phase angle of every single frequency in the current spectrum, although only the values for the test signal frequency are needed. The Goertzel algorithm is therefore implemented, which only computes phase and amplitude of a requested harmonic. If the number of computed harmonics M is less than $\log_2 N$, (N is the number of samples), the Goertzel algorithm has less computational effort than a Fast Fourier Transformation [23], but delivers the same results for the requested harmonic. If the amplitude and phase angle of more than one signal are needed, as in the present case, this advantage of the Goertzel algorithm increases.

The Goertzel algorithm is applied to the real and imaginary part of \vec{I}_{res} (Fig. 1). It delivers the amplitudes $\hat{i}_{hf\alpha}$ and $\hat{i}_{hf\beta}$ of the corresponding signals, as well as the associated phase angles (not depicted). In order to calculate the fundamental waveform current \vec{I}_1 , the high-frequency current waveforms $I_{hf\alpha}$ and $I_{hf\beta}$ are reconstructed. According to (5) the subtraction of the measured current space vector \vec{I}_{res} and the test signal current \vec{I}_{hf} provides the desired current \vec{I}_1 .

$$I_{1\alpha} = I_{res\alpha} - I_{hf\alpha} \quad (6)$$

$$I_{1\beta} = I_{res\beta} - I_{hf\beta} \quad (7)$$

Consequently, the test signal injection and analysis are decoupled from the heterodyned field-oriented control.

IV. DEPENDENCIES OF COMPLEX HF-IMPEDANCE

Detailed investigations have shown that the measured complex impedance depends on numerous impacts [15]. The research was made on a 15 kW standard induction motor with two pole pairs, forty-eight slots in the stator and thirty-six rotor slots, whereof twelve are opened and

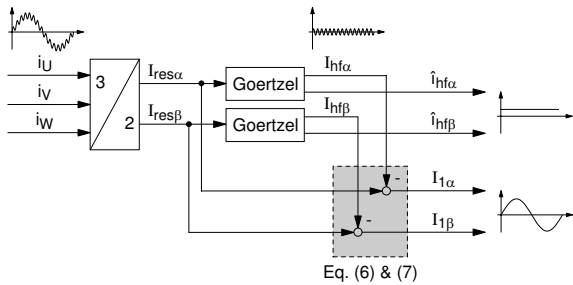


Fig. 1: Topology of the current separation scheme

twenty-four are closed. The machine design was changed in neither the stator nor in the rotor. The investigations concluded FE calculations which were made with the FE program FLUX2D [24]. A magnetic equivalent circuit for the high-frequency flux, including the skewing of the rotor, was also derived in order to investigate the machine's high-frequency behaviour in detail.

The investigations have shown that the measured complex high-frequency impedance, as defined in (3), depends on the mechanical angle of the rotor φ_{mech} , the slip frequency f_2 , the angle of the stator current space vector in the stator fixed coordinate system φ_1 and the test signal angle α . In the case of nominal flux every impedance curve is unique, and can therefore be measured and described as

$$\underline{Z} = f(\varphi_1, \alpha, f_2, \varphi_{mech}) \quad (8)$$

These reference impedance curves can be measured while the induction motor is magnetised by a DC stator current and the mechanical velocity is determined by a speed-controlled machine, which is coupled on the motor shaft. A field-oriented control provides through the DC current nominal flux in the induction motor. The slip frequency f_2 can be calculated via:

$$f_2 = f_1 - p \cdot n \quad (9)$$

wherein f_1 is the stator frequency, p is the number of pole pairs and n is the mechanical velocity. Thus, in the presence of DC stator current ($f_1 = 0$ Hz), the slip frequency f_2 and the mechanical angle φ_{mech} are determined by the load machine and can be measured directly, whereas the parameters φ_1 and α can be chosen.

Fig. 2 shows a measured impedance curve of the investigated machine at standstill and nominal flux ($\varphi_1 = 0^\circ$). The dependency on the mechanical angle and the test signal angle, as well as the 30° -periodicity with reference to φ_{mech} owing to the opened and closed rotor slots, becomes visible. Fig. 3 shows clearly, that even a slight change in the mechanical angle of the rotor φ_{mech} leads to a different impedance curve. The magnitude value as well as the angle at which this maximum appears changes.

Because of the large number of impacts on the complex impedance, a new estimation method for the mechanical speed of the induction motor was developed.

V. ESTIMATION METHOD

As shown above, the complex impedance is also adicted to the slip frequency f_2 . Consequently, the slip frequency of the induction machine can be calculated via a comparison between the measured reference curves in the presence of DC magnetisation as described in section IV and the actual measured impedance values during the machine's operation. By the way of explanation the induction motor should first be magnetised by a DC current to its nominal rotor flux level and operate at a constant mechanical speed. Later, it will be shown that the consideration of a rotating field is only a small step.

During the machine's operation the test signal as described by (1) is added to the demanded voltages of the

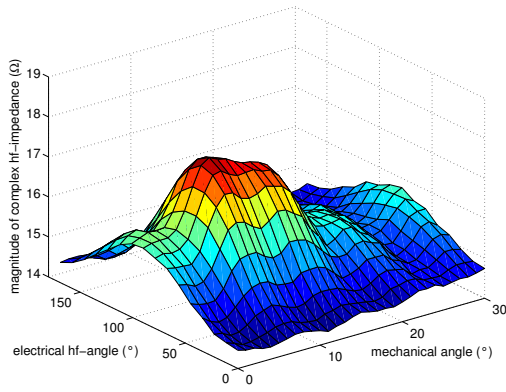


Fig. 2: Measured hf-impedance at standstill and magnetisation to nominal rotor flux in α -direction

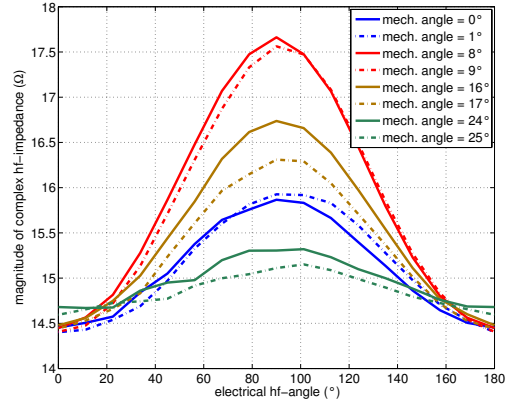


Fig. 3: Curves of measured hf-impedance of Fig. 2 for different mechanical angles

field-oriented control as illustrated in Fig. 4. The resulting test signal current is extracted for the calculation of the complex impedance \underline{Z} as explained in section III. The measured value of the complex impedance is stored in the array \underline{Z}_{meas} with k elements, wherein the currently measured value is on the first position, and the latest on the last. Although the test signal has an alternating nature, it rotates in the stator fixed coordinate system with a fixed frequency, in order to measure the complex impedance for different test signal angles.

A measured impedance curve while the machine is in operation is shown in Fig. 5. The machine was, as described above, magnetised by a DC current. While the impedance was measured, the machine rotated with $n = 6 \text{ min}^{-1}$ and the angle of the stator current φ_1 was zero (α -direction). Between the measurement of a single impedance value a small time delay Δt was inserted.

The angle of the magnetising DC current space vector in the stator can be measured easily. The angle of the test signal of every measured value and the time space between the single measurements Δt are also known. For

constant speed, only the mechanical angle φ_{mech} of the last measured impedance value and the slip frequency f_2 are therefore the unknown parameters.

$$\underline{Z} = f\left(\underbrace{\varphi_1}_{\text{measured}}, \underbrace{\alpha}_{\text{given}}, \underbrace{f_2, \varphi_{mech}}_{\text{unknown}}\right) \quad (10)$$

For a fixed pair of a proposed mechanical angle φ'_{mech} and a proposed slip frequency f'_2 , the mechanical angles of all measured impedance values can be computed. From (9) follows:

$$\varphi_{mech} = 2\pi \int \left(\frac{f_1 - f_2}{p}\right) dt \quad (11)$$

The changing of the mechanical angle as a consequence of the slip frequency can be described by

$$\Delta\varphi'_2(\nu) = \nu \cdot \frac{2\pi \cdot f'_2}{p} \cdot \Delta t \quad (12)$$

with ν as the counting value starting with 0 (current measured value). According to (11), the mechanical angles of the measured values in the absence of a rotating field ($f_1 = 0 \text{ Hz}$) can be calculated via

$$\varphi'_{mech}(\nu) = \varphi'_{mech} + \Delta\varphi'_2(\nu) \quad (13)$$

Afterwards, the differences between the magnitude of the measured values and their opposites in the belonging reference curve are calculated. An error value is defined as follows:

$$\epsilon(\varphi'_{mech}, f'_2) = \sum_{\nu} \left| |\underline{Z}_{meas}(\nu)| - |\underline{Z}_{ref}| \right| \quad (14)$$

with

$$\underline{Z}_{ref} = \underline{Z}_{ref}(\varphi_1(\nu), \alpha(\nu), f'_2, \varphi'_{mech}(\nu)) \quad (15)$$

This error value is calculated for several combinations of φ'_{mech} and f'_2 . The combination of φ'_{mech} and f'_2 for which

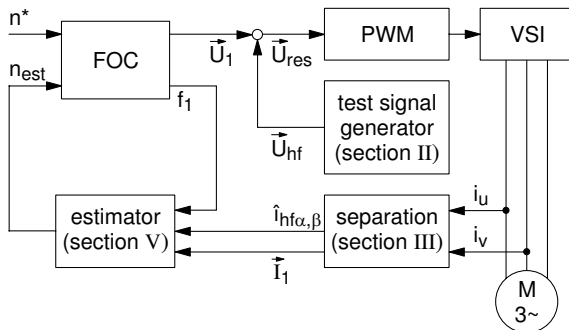


Fig. 4: Topology of the sensorless field-oriented control (FOC) with alternating test signal

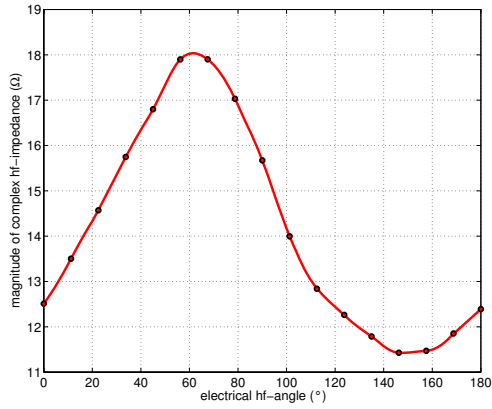


Fig. 5: Measured hf-impedance values (marker) at $n = 6 \text{ min}^{-1}$, DC nominal flux and $\varphi_1 = 0^\circ$ while machine is in operation

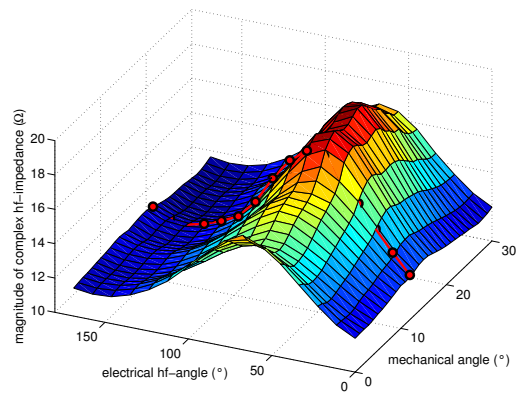


Fig. 6: Reference impedance face for $f_2 = -0, 2 \text{ min}^{-1}$, DC nominal flux and $\varphi_1 = 0^\circ$ and measured values of Fig. 5 (red)

the error ϵ has a minimum, corresponds to the current mechanical values of the machine, and represents therefore the estimated values.

$$\min \left(\epsilon \left(\varphi'_{mech}, f'_2 \right) \right) \rightarrow \varphi_{mech}, f_2 \quad (16)$$

In the case of the measured values depicted in Fig. 5, the associated combination is $\varphi_{mech} = 17^\circ$ and $f_2 = -0, 2 \text{ Hz}$ as shown in Fig. 6.

In the next step the rotating magnetic field has to be taken into account. It is clear that it has to be considered in the selection of \underline{Z}_{ref} (15), but also in (13). Note that the equation only takes the slip frequency f_2 into account, and not the rotating field. The changing of the angle of the rotating field relative to the actual value can be described by:

$$\Delta\varphi_1(\nu) = \frac{\varphi_1(0) - \varphi_1(\nu)}{p} \quad (17)$$

Thus, the proposed mechanical angle of the measured impedance values can be calculated via

$$\varphi'_{mech}(\nu) = \varphi'_{mech} + \Delta\varphi_2(\nu) - \Delta\varphi_1(\nu) \quad (18)$$

The described method delivers the mechanical angle φ_{mech} and the slip frequency f_2 , which are two independent values of the algorithm. In order to get the demanded mechanical velocity, (9) can be evaluated, wherein f_1 is the frequency of the rotor flux, which is a known value in a field-oriented control.

$$n = \frac{1}{p} \cdot \left(\underbrace{f_1}_{\text{known}} - \underbrace{f_2}_{\text{estimated}} \right) \quad (19)$$

Another method is to differentiate the estimated mechanical angle. In practice the differentiation doesn't lead to satisfactory results because of the non-smooth nature of the estimated angle. The first option (evaluation of (19)) is therefore used.

VI. ROTATING TEST SIGNAL

When the machine is excited by a test signal with alternating nature (1), every change in the test signal angle α induces a transient response of the system. In order to get the steady-state value of the complex impedance (3), a delay time Δt must be inserted between the angle's changing and the measurement of \underline{Z} . This delay time can be reduced by use of a rotating test signal. The measurement effort for the reference impedance curves can also be reduced.

The alternating test signal (1) can be described by two rotating signals, a positive and a negative phase-sequence voltage, \vec{U}_{hf}^+ and \vec{U}_{hf}^- .

$$\vec{U}_{hf} = \hat{U}_{hf} \cdot \cos(\omega_{hf}t) \cdot e^{j\alpha} \quad (20)$$

$$= \vec{U}_{hf}^+ + \vec{U}_{hf}^- \quad (21)$$

The voltages follow the equations:

$$\vec{U}_{hf}^+ = \frac{\hat{U}_{hf}}{2} \cdot e^{j(+\omega_{hf}t + \alpha)} \quad (22)$$

$$\vec{U}_{hf}^- = \frac{\hat{U}_{hf}}{2} \cdot e^{j(-\omega_{hf}t + \alpha)} \quad (23)$$

All values in the positive phase-sequence system are marked by a '+', those of the negative phase-sequence system with a '-' as exponent.

The positive and negative phase-sequence space vector voltages are generated, according to the space vector theory, by the superposition of the phase-to-neutral voltages u_U , u_V and u_W :

$$u_U^\pm = \frac{\hat{U}_{hf}}{2} \cdot \cos(\pm\omega_{hf}t + \alpha) \quad (24)$$

$$u_V^\pm = \frac{\hat{U}_{hf}}{4} \left(\begin{array}{l} +\sqrt{3} \sin(\pm\omega_{hf}t + \alpha) \\ -\cos(\pm\omega_{hf}t + \alpha) \end{array} \right) \quad (25)$$

$$u_W^\pm = \frac{\hat{U}_{hf}}{4} \left(\begin{array}{l} -\sqrt{3} \sin(\pm\omega_{hf}t + \alpha) \\ -\cos(\pm\omega_{hf}t + \alpha) \end{array} \right) \quad (26)$$

wherein $u_{\bar{U}}^{\pm}$, $u_{\bar{V}}^{\pm}$ and $u_{\bar{W}}^{\pm}$ describe the positive and negative phase-sequence phase-to-neutral voltages. Note that the test signal angle α acts in all equations like a time-shift.

$$\alpha = \omega_{hf} t_0 \quad (27)$$

At high-frequency excitation the corresponding hf-flux does not penetrate the rotor cage, but distributes on the rotor's surface. The vector of the phase-to-neutral voltages at the machine terminals \mathbf{u}_m can therefore be described as follows:

$$\mathbf{u}_m = \mathbf{R} \cdot \mathbf{i} + \mathbf{M} \cdot \mathbf{i}' \quad (28)$$

with \mathbf{i}' as the derivation of \mathbf{i} and

$$\mathbf{u}_m = \begin{bmatrix} u_{Um} \\ u_{Vm} \\ u_{Wm} \end{bmatrix} \quad (29)$$

$$\mathbf{i} = \begin{bmatrix} i_U \\ i_V \\ i_W \end{bmatrix} \quad (30)$$

$$\mathbf{R} = \begin{bmatrix} R_U & 0 & 0 \\ 0 & R_V & 0 \\ 0 & 0 & R_W \end{bmatrix} \quad (31)$$

$$\mathbf{M} = \begin{bmatrix} L_U & M_{UV} & M_{UW} \\ M_{VU} & L_V & M_{VW} \\ M_{WU} & M_{WV} & L_W \end{bmatrix} \quad (32)$$

wherein R_U , R_V and R_W are the resistances and L_U , L_V and L_W are the self-inductances of the associated phase. The couplings between the phases are considered by M .

Note that the phase-to-neutral voltages of the machine may differ from the inverter voltages as described in (24) - (26), because of the unsymmetrical hf-behaviour of the machine. Thus, in the case of a star-connected machine, a voltage u_0 between the two neutral points can be measured. The machine voltages (marked by the index m) can be expressed by the inverter voltages and the voltage between the neutral points of the machine and the inverter u_0 (Fig. 7).

$$u_{Um}^{\pm} = u_{\bar{U}}^{\pm} - u_0 \quad (33)$$

$$u_{Vm}^{\pm} = u_{\bar{V}}^{\pm} - u_0 \quad (34)$$

$$u_{Wm}^{\pm} = u_{\bar{W}}^{\pm} - u_0 \quad (35)$$

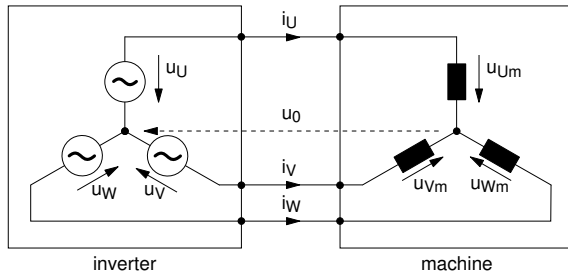


Fig. 7: Voltages and currents of the inverter and the machine

Thus, equation (28) can be expressed by:

$$\begin{bmatrix} u_{\bar{U}}^{\pm} - u_0 \\ u_{\bar{V}}^{\pm} - u_0 \\ u_{\bar{W}}^{\pm} - u_0 \end{bmatrix} = \mathbf{R} \cdot \mathbf{i}^* + \mathbf{M} \cdot (\mathbf{i}^*)' \quad (36)$$

with

$$\mathbf{i}^* = \begin{bmatrix} i_{\bar{U}}^{\pm} \\ i_{\bar{V}}^{\pm} \\ -i_{\bar{U}}^{\pm} - i_{\bar{V}}^{\pm} \end{bmatrix} \quad (37)$$

Finally, the voltages of the two meshes in Fig. 7 can be calculated by:

$$\begin{aligned} u_{\bar{U}}^{\pm} - u_{\bar{V}}^{\pm} &= R_U \cdot i_{\bar{U}}^{\pm} - R_V \cdot i_{\bar{V}}^{\pm} + \\ &+ \frac{di_{\bar{U}}^{\pm}}{dt} \cdot (L_U - M_{VU} - M_{UW} + M_{VW}) \\ &+ \frac{di_{\bar{V}}^{\pm}}{dt} \cdot (M_{UV} - L_V - M_{UW} + M_{VW}) \end{aligned} \quad (38)$$

and

$$\begin{aligned} u_{\bar{V}}^{\pm} - u_{\bar{W}}^{\pm} &= R_W \cdot i_{\bar{U}}^{\pm} + (R_V + R_W) \cdot i_{\bar{V}}^{\pm} + \\ &+ \frac{di_{\bar{U}}^{\pm}}{dt} \cdot (M_{VU} - M_{WU} - M_{VW} + L_W) \\ &+ \frac{di_{\bar{V}}^{\pm}}{dt} \cdot (L_V - M_{WV} - M_{VW} + L_W) \end{aligned} \quad (39)$$

wherein the voltages are described by (24) - (26) and the resistances and reactances are determined by the machine.

The phase currents $i_{\bar{U}}^{\pm}$, $i_{\bar{V}}^{\pm}$ and $i_{\bar{W}}^{\pm}$ can be calculated by the application of the Laplace transformation on (38) and (39). In the following, only the Laplace transformed $I_{\bar{U}}^{\pm}(s)$ of the positive phase-sequence line current $i_{\bar{U}}^{\pm}$ is examined, but the results can also be assigned to the other currents. The transient part of the current $i_{\bar{U}}^{\pm}$ is also neglected, since the test signal is applied during the whole machine's operation and thus the general solution is zero.

In the case of steady-state behaviour, the test signal angle α can be neglected for the transformation of the phase voltages $u_{\bar{U}}^{\pm}$, $u_{\bar{V}}^{\pm}$ and $u_{\bar{W}}^{\pm}$, since it acts like a time-shift (27). This time-shift, and thus the test signal angle, can be considered in the current's solution. The steady-state behaviour of $i_{\bar{U}}^{\pm}$ in the Laplace transformation follows the equation:

$$I_{\bar{U}}^{\pm}(s) = c_1 \cdot \frac{s + c_2}{s^2 + \omega_{hf}^2} \quad (40)$$

wherein c_1 and c_2 are constants, which depend on the test signal parameters as well as on the machine's resistances and reactances. The transformation of (40) to the time domain and the consideration of the test signal angle (27) leads to:

$$i_{\bar{U}}^{\pm}(t) = c_0 \cdot \sin(\omega_{hf} t + \phi + \alpha) \quad (41)$$

wherein

$$c_0 = c_1 \cdot \sqrt{1 + \frac{c_2^2}{\omega_{hf}^2}} \quad (42)$$

$$\tan \phi = \frac{\omega_{hf}}{c_2} \quad (43)$$

$$c_1 = f(\omega_{hf}, R_U, \dots) \quad (44)$$

$$c_2 = f(\omega_{hf}, R_U, \dots) \quad (45)$$

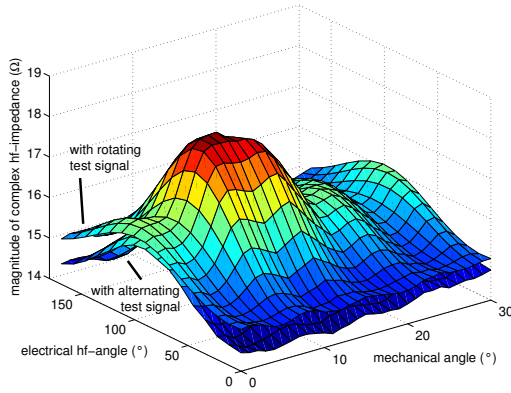


Fig. 8: Measured impedance curves for standstill, nominal DC flux with alternating (Fig. 2) and rotating test signal

Note that c_0 and ϕ are measured values (e.g. FFT or Goertzel of i_U^+), and that the test signal angle α is a choosable input value. Thus, with a single measurement of c_0 and ϕ , i_U^+ can be calculated for every test signal angle.

From (41) - (45), it becomes obvious that the amplitude c_0 as well as the phase angle ϕ of the phase current also depends on the test signal frequency and amplitude. Because of the frequency dependency of c_1 and c_2 the negative phase-sequence current cannot be exactly calculated if only the positive phase-sequence current is applied to the machine. But in practice these differences are small and thus the amplitude c_0 and the phase angle ϕ are similar for i_U^+ and i_U^- .

Fig. 8 depicts the complex impedance curve while the measurement was made with a rotating test signal. Only the positive phase-sequence test signal voltage was applied to the machine. Only the corresponding positive phase-sequence current was therefore measured. The calculation of the negative phase-sequence current was made on the assumption that c_1 and c_2 , and consequently c_0 and ϕ , are equal for both currents.

$$i_U^-(t) = c_0 \cdot \sin(-\omega_{hf}t + \phi + \alpha) \quad (46)$$

The addition of the measured positive phase-sequence current space vector and the calculated negative phase-sequence current leads to a fictitious current which corresponds to a test signal as described by (21).

$$\vec{I}_{hf}^\pm = \frac{2}{3} \cdot (i_U^\pm + \underline{a} \cdot i_V^\pm + \underline{a}^2 \cdot i_W^\pm) \quad (47)$$

$$\vec{I}_{hf} = \vec{I}_{hf}^+ + \vec{I}_{hf}^- \quad (48)$$

As already indicated, the calculated negative phase-sequence current is different from that actually measured with an alternating test signal, because of the different values of c_1 and c_2 for i_U^+ and i_U^- . The resulting high-frequency current of (48) is also therefore not equal to that actually measured.

The comparison of the shape of the complex impedance, measured with an alternating test signal, with

the shape for the measurement with the rotating test signal shows that the error is very small (Fig. 8). Indeed, the absolute values are slightly smaller in the case of the alternating test signal but, and this is remarkable, the shape of the impedance curve is preserved. Thus, if the reference impedance curves are measured in the described manner, the proposed method (section V) also works with the rotating test signal.

The advantage of the rotating test signal is the strong reduced measurement effort for the reference curves. With the alternating test signal, the complex impedance for every combination of test signal angle α and mechanical angle φ_{mech} for a fixed combination of φ_1 and f_2 have to be measured. With the rotating test signal, only c_0 and ϕ has to be measured for every mechanical angle. The curve over the test signal angle α can be calculated as described above. When the complex impedance is measured for every 10° of α , the measurement amount is reduced to the seventeenth part when the rotating test signal is used.

VII. EXPERIMENTAL RESULTS

The proposed method using the rotating test signal was implemented on a dSPACE-System and tested on two different induction machines (technical data in Tab. I). The detailed investigations were made on machine 1. Machine 2 is an induction machine, of which no further technical data (shape of lamination, number of slots, etc.) are known. Both machines are standard induction motors, which are not specially designed for sensorless control, and which are not manipulated in order to show special behaviour.

The topology of the sensorless control is depicted in Fig. 9. Instead of the alternating test signal, only the positive phase-sequence voltage

$$\vec{U}_{hf}^+ = \frac{\hat{U}_{hf}}{2} \cdot e^{j(\omega_{hf}t)} \quad (49)$$

is added to the voltage \vec{U}_1 , which is demanded by the field-oriented control. Note that α does not appear in (49), because it only acts as a time-shift. The test signal angle is important for the calculation of the alternating high-frequency current \vec{I}_{hf} as described in section VI. The

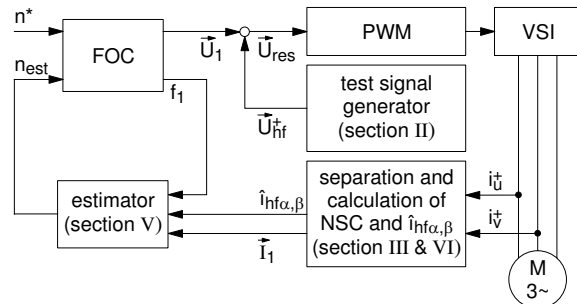


Fig. 9: Topology of the sensorless field-oriented control (FOC) with rotating test signal and calculation of negative phase-sequence current (NSC)

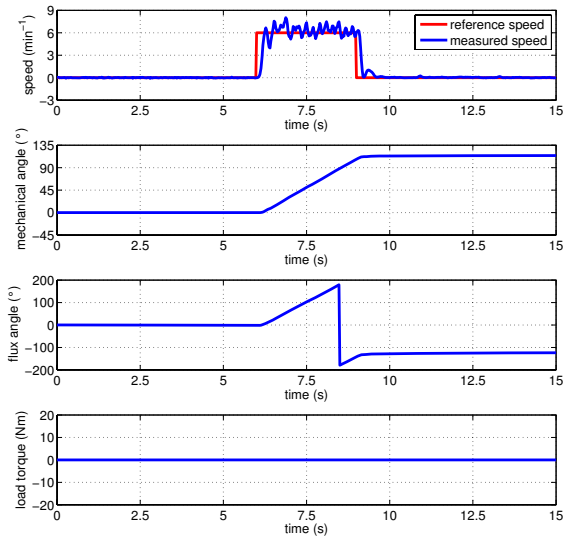


Fig. 10: **Machine 1**, sensorless control: response to steps of the reference speed at no-load operation

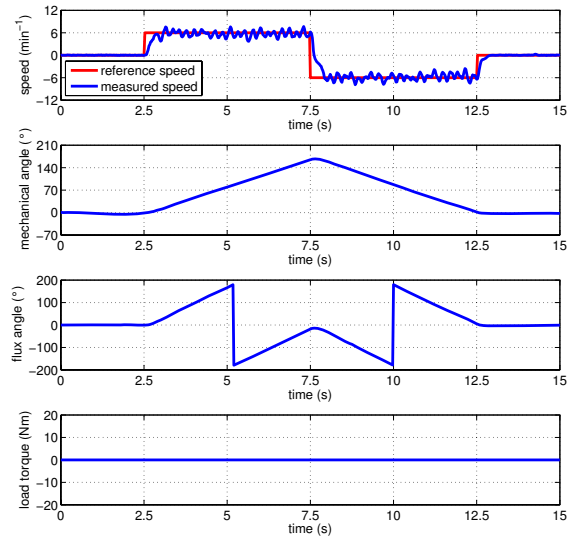


Fig. 11: **Machine 1**, sensorless control: response to steps of the reference speed while operating at no-load

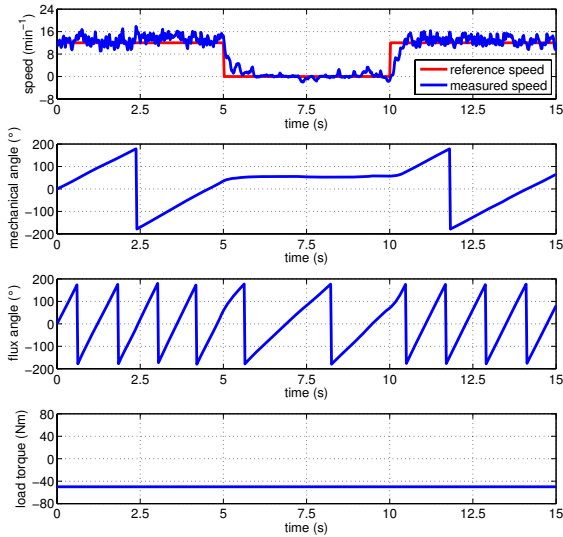


Fig. 12: **Machine 1**, sensorless control: response to steps of the reference speed while operating at 50 Nm (50% of nominal torque)

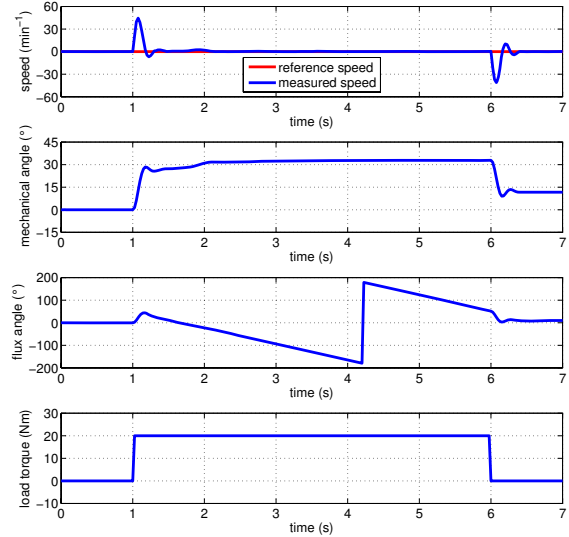


Fig. 13: **Machine 1**, sensorless control: response to steps of the load torque (20% of nominal torque) while operating at zero speed

results using the alternating test signal were published in [15].

A. Machine 1

Figs. 10 - 13 show the behaviour of the sensorless control of machine 1. The responses to steps in the reference speed at no-load operation are depicted in Figs. 10 and 11. It becomes obvious that the proposed method allows save operation even at standstill and zero frequency.

In addition, the sensorless control can handle loads up to 50% of the nominal torque (Fig. 12), and also load steps at standstill can be controlled precisely (Fig. 13).

B. Machine 2

The step responses of the sensorless control of machine 2 are shown in Figs. 14 - 17. In Figs. 14 and 15 the machine operated at no-load. The behaviour under constant loaded conditions and under load steps is shown in

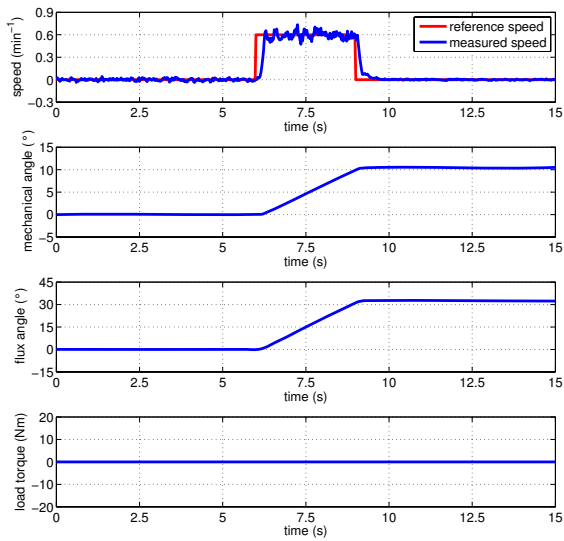


Fig. 14: **Machine 2**, sensorless control: response to steps of the reference speed at no-load operation

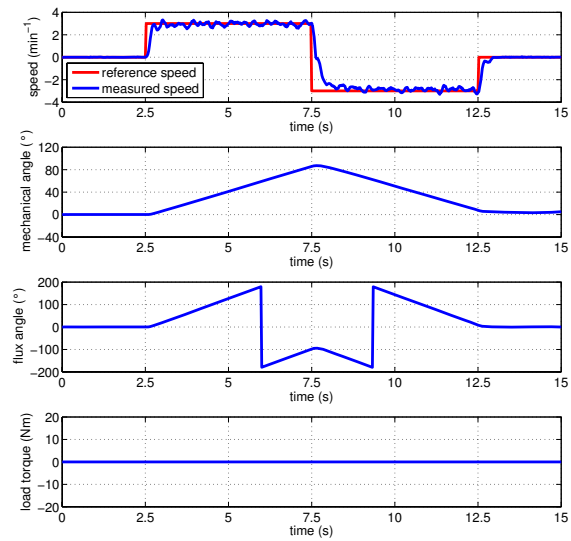


Fig. 15: **Machine 2**, sensorless control: response to steps of the reference speed while operating at no-load

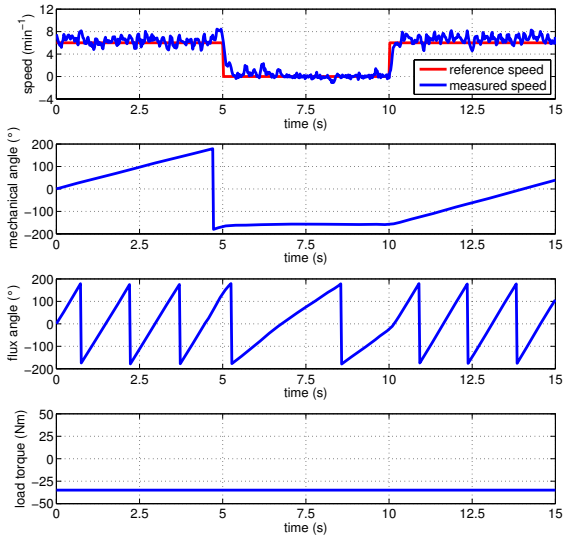


Fig. 16: **Machine 2**, sensorless control: response to steps of the reference speed while operating at 35 Nm (40% of nominal torque)

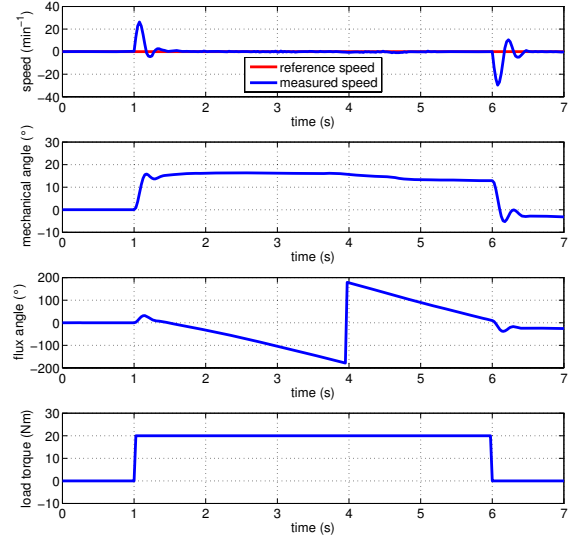


Fig. 17: **Machine 2**, sensorless control: response to steps of the load torque (20% of nominal torque) while operating at zero speed

Figs 16 and 17. Thus, in the case of the second machine also, the proposed method allows save and precise machine operation even at standstill and zero frequency.

VIII. CONCLUSION

With the help of a test signal a complex impedance can be measured which depends on numerous impacts. Hitherto, the separation of these phenomena was fundamental in order to extract e.g. the mechanical speed or the

flux angle. Since separation is not always possible, a new method was developed that allows sensorless field-oriented control of machines with multiple non-separable or single saliencies without the introduction of an additional sensor.

Since the measured impedance curves are unique, the method is based on the comparison of the impedance curve measured during the machine's operation with precommissioned reference impedance curves. The combination of the slip frequency f_2 and the mechanical angle φ_{mech} for

which the error between these two curves is the lowest represents the actual values. The proposed method allows save machine operation at standstill (loaded and unloaded) and even at zero frequency. It was tested on two different induction machines.

In order to reduce the precommissioning effort, the alternating test signal was exchanged for a rotating test signal. Only the positive phase-sequence voltage of the test signal with alternating nature is applied to the machine, and the negative phase-sequence current is calculated. The calculated negative phase-sequence current differs from that actually measured with the alternating test signal, but only slightly in the absolute value of the complex impedance. The shape of the complex impedance curve therefore does not change. It was shown that the method works also with the rotating test signal.

The author is now testing the performance of the presented sensorless control on different induction machines from a few hundred W to a few kW. The proposed method will also be tested on synchronous motors with permanent magnets (buried and surface mounted), as well as on synchronous motors with tooth coils, because the dependence of the complex impedance on the load and the mechanical angle also exists in these machines. The first measurements are very promising.

APPENDIX

TABLE I: Technical data of the used induction motors

	machine 1	machine 2
nominal power, P_N	15 kW	11 kW
nominal voltage, U_N	400 V, Y	400 V, Δ
nominal current, I_N	28,6 A	22 A
nominal frequency, f_N	50 Hz	60 Hz
number of pole pairs, p	2	3

REFERENCES

[1] C. Schauder, "Adaptive speed identification for vector control of induction motors without rational transducers," *IEEE Transactions on Industry Applications*, vol. 28, no. 5, pp. 1054–1061, 1992.

[2] K. Ohyama, G. M. Asher, and M. Sumner, "Comparative analysis of experimental performance and stability of sensorless induction motor drives," *IEEE Transactions on Industrial Electronics*, vol. 53, no. 1, pp. 178–186, 2006.

[3] C. Lascu, I. Boldea, and F. Blaabjerg, "Comparative study of adaptive and inherently sensorless observers for variable-speed induction-motor drives," *IEEE Transactions on Industrial Electronics*, vol. 53, no. 1, pp. 57–65, 2006.

[4] T. Orłowska-Kowalska, "Rotor flux observer and speed estimators for sensorless induction motor drives - comparative study," *Proceedings of International Power Electronics and Motion Control Conference (EPE-PEMC)*, Dubrovnik and Cavtat, Croatia, 2002.

[5] P. Vas, *Sensorless vector and direct torque control*. Oxford: Oxford University Press, 1998.

[6] T. M. Wolbank, J. L. Machl, H. Hauser, and P. Macheiner, "Anisotropy in induction machine lamination and its influence on mechanical sensorless control and condition monitoring," *Proceedings of European Conference on Power Electronics and Applications (EPE)*, Toulouse, France, 2003.

[7] J. Holtz, "Sensorless control of induction machines - with or without signal injection?," *IEEE Transactions on Industrial Electronics*, vol. 53, no. 1, pp. 7–30, 2006.

[8] M. Schrödl, "Sensorless control of ac machines at low speed and standstill based on the "inform" method," *Conference Record of the 1996 IEEE Industry Applications Conference*, pp. 270–277, 1996.

[9] C. S. Staines, G. M. Asher, and M. Sumner, "Rotor-position estimation for induction machines at zero and low frequency utilizing zero-sequence currents," *IEEE Transactions on Industry Applications*, vol. 42, no. 1, pp. 105–112, 2006.

[10] C. Caruana, G. M. Asher, and M. Sumner, "Performance of hf signal injection techniques for zero-low-frequency vector control of induction machines under sensorless condition," *IEEE Transactions on Industrial Electronics*, vol. 53, no. 1, pp. 225–238, 2006.

[11] A. Consoli, G. Scarcella, G. Bottiglieri, G. Scelba, A. Testa, and D. A. Triolo, "Low-frequency signal-demodulation-based sensorless technique for induction motor drives at low speed," *IEEE Transactions on Energy Conversion*, vol. 53, no. 1, pp. 20–215, 2006.

[12] P. L. Jansen and R. D. Lorenz, "Transducerless field orientation concepts employing saturation-induced saliencies in induction machines," *IEEE Transactions on Industry Applications*, vol. 32, no. 6, pp. 1380–1393, 1996.

[13] M. L. Aime, M. W. Degner, and R. D. Lorenz, "Saturation measurements in ac machines using carrier signal injection," *IEEE Industry Application Society Annual Meeting*, 1998.

[14] R. D. Lorenz, "Practical issues and research opportunities when implementing zero speed sensorless control," *Proceedings of International Conference on Electric Machines and Systems (ICEMS)*, Shenyang, China, 2001.

[15] H. Zatocil, "Physical understanding of multiple saliencies in induction motors and their impact on sensorless control," *SPEEDAM*, Ischia, Italy, 2008.

[16] A. Consoli, G. Scarcella, and A. Testa, "An alternative to high frequency current detection techniques for zero speed sensorless control of ac motor drives," *Proceedings of International Power Electronics and Motion Control Conference (EPE-PEMC)*, Dubrovnik and Cavtat, Croatia, 2002.

[17] A. Consoli, G. Scarcella, G. Bottiglieri, and A. Testa, "Harmonic analysis of voltage zero-sequence-based encoderless techniques," *IEEE Transactions on Industry Applications*, vol. 42, no. 6, pp. 1548–1557, 2006.

[18] J.-I. Ha, S.-K. Sul, K. Ide, I. Murokita, and K. Sawamura, "Physical understanding of high frequency injection method to sensorless drives of an induction machine," *IEEE Industry Application Society Annual Meeting*, 2000.

[19] A. Consoli, G. Scarcella, G. Tutino, and A. Testa, "Finite element analysis of flux angle estimation techniques based on high frequency signal injection," *Proceedings of International Symposium on Power Electronics, Electrical Drives, Automation & Motion (SPEEDAM)*, pp. 1–6, Ischia, Italy, 2000.

[20] D. Drevensek, D. Zarko, and T. A. Lipo, "A study of sensorless control of induction motor at zero speed utilizing high frequency voltage injection," *Proceedings of International Power Electronics and Motion Control Conference (EPE-PEMC)*, Dubrovnik and Cavtat, Croatia, 2002.

[21] T. M. Wolbank, R. Wöhrnschimmel, and J. L. Machl, "Slot geometry - an important design parameter for zero speed sensorless control of standard induction machines," *Proceedings of International Power Electronics and Motion Control Conference (EPE-PEMC)*, Dubrovnik and Cavtat, Croatia, 2002.

[22] T. M. Wolbank and R. Wöhrnschimmel, "Influence of rotor design on sensorless control for induction motors," *EPE*, Graz, Austria, 2001.

[23] A. V. Oppenheim and R. W. Schaffer, *Discrete-time signal processing*. New Jersey: Prentice Hall, 2 ed., 1999.

[24] FLUX2D, *User's guide*, vol. 1-5. Grenoble: CEDRAT, 2006.